
Article:
Saidi, Norshahirah M., Omar, Fatin Saiha, Numan, Arshid et al. (5 more authors) (2019) Enhancing the Efficiency of a Dye-Sensitized Solar Cell Based on a Metal Oxide Nanocomposite Gel Polymer Electrolyte. ACS Appl Mater Interfaces. 30185–30196. ISSN 1944-8252

https://doi.org/10.1021/acsami.9b07062

Enhancing Efficiency in a Dye-Sensitized Solar Cell Based on a Metal Oxide Nanocomposite Gel Polymer Electrolyte

Norshahirah M. Saidi[a], Fatin Saiha Omar[a], Arshid Numan[b], David C. Apperley[c], Mohammed M. Algaradah[c], Ramesh Kasi[a], Alyssa-Jennifer Avestro*[c,d], Ramesh T. Subramaniam*[a]

[a]Centre for Ionics University of Malaya, Department of Physics, University of Malaya, Kuala Lumpur 50603, Malaysia

[b]State Key Laboratory of ASIC and System, SIST, Fudan University, 200433, Shanghai, China

[c]Department of Chemistry, Science Site, Stockton Road, Durham University, Durham DH1 3LE, United Kingdom

[d]Department of Chemistry, University of York, Heslington, York YO10 5DD, United Kingdom

KEYWORDS Gel Polymer Electrolytes, Dye-Sensitized Solar Cells, Metal Oxide Nanoparticles, Current Density, Efficiency

ABSTRACT: In order to overcome the critical limitations of liquid electrolyte-based dye-sensitized solar cells, quasi-solid-state electrolytes have been explored as a means of addressing long-term device stability, albeit with comparatively low ionic conductivities and device performances. Although metal oxide additives have been shown to augment ionic conductivity, their propensity to aggregate into large crystalline particles upon high-heat annealing hinders their full potential in quasi-solid-state electrolytes. In this work, sonochemical processing has been successfully applied to generate fine Co_3O_4 nanoparticles that are highly dispersible in a PAN:P(VP-*co*-VAc) polymer blended gel electrolyte, even after calcination. An optimized nanocomposite gel polymer electrolyte containing 3 wt% sonicated Co_3O_4 nanoparticles (PVVA-3) delivers the highest ionic conductivity (4.62 x 10^{-3} S cm^{-1}) of the series. This property is accompanied by a 51% enhancement in the apparent diffusion coefficient of triiodide versus both unmodified and unsonicated electrolyte samples. The dye-sensitized solar cell based on PVVA-3 displays a power conversion efficiency of 6.46% under AM1.5G, 100 mW cm^{-2}. By identifying the optimal loading of sonochemically processed nanoparticles, we are able to generate a homogenous extended particle network that effectively mobilizes redox active species through a highly amorphous host matrix. This effect is manifested in a selective 51% enhancement in photocurrent density (J_{SC} = 16.2 mA cm^{-2}) and a lowered barrier to N719 dye regeneration (R_{CT} = 193 Ω) versus an unmodified solar cell. To the best of our knowledge, this work represents the highest known efficiency to-date for dye-sensitized solar cells based on a sonicated Co_3O_4-modified gel polymer electrolyte. Sonochemical processing, when applied in this manner, has the potential to make meaningful contributions towards the ongoing mission to achieve the widespread exploitation of stable and low-cost dye-sensitized solar cells.

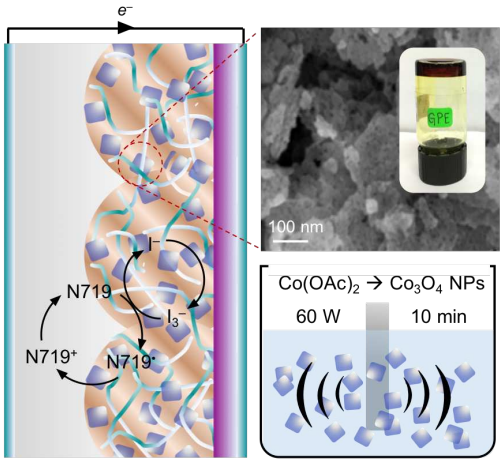

1. INTRODUCTION

Ever since the first report of dye-sensitized solar cells (DSSCs) by O'Regan and Grätzel[1] in 1991, energy conversion efficiencies have experienced a steady upward trend, approaching 14% for liquid electrolyte (LE)-based cells.[2] Though they still lag in terms of efficiency compared to more other solid-state photovoltaics, the theoretical price–performance ratio of these simple thin-film devices make DSSCs highly attractive candidates for achieving global grid parity[3] against fossil fuels. Their wider scale implementation has been delayed, however, by a number of critical issues including degradation, cell leakage, dye desorption, thermal instability, and electrode corrosion—all of which can be traced back to the use of traditional LEs.[4-7] As a result, research efforts have been focused on replacing conventional LE media with other suitable alternatives, such as ionic liquids[8–13], solid-state perovskites[14–17], and solid/quasi-solid-state polymer gels and their composites.[8–34]

Gel polymer electrolytes (GPEs) have received considerable attention in recent years due to their straightforward formulation into thermally and mechanically robust solids and quasi-solids that overcome many drawbacks of LEs.[7] To date, optimized DSSCs based on GPEs can achieve efficiencies as high as 9.61%.[33] Poly(acrylonitrile) (PAN) is a popular component of GPEs that typically provides a high

Table 1. Literature Performance Parameters[a] of DSSCs Based on Metal Oxide-Nanocomposite GPEs

Additive[b] (wt%)	GPE Matrix[c] (Solvent[d])	σ / 10^{-4} S cm^{-1}	J_{SC} / mA cm^{-2}	V_{OC} / V	η / %	ref
TiO_2 (–)[e]	PEO/TBP/LiI/I_2 (EC:PC:MeCN)	—[e]	3.77	0.61	5.05	54
TiO2 (2)	PMMA/KI/I_2 (PC)	1.75	6.08	0.62	2.34	55
TiO_2 (2.5)	Agarose/LiI/I_2 (NMP)	4.40	10.96	0.55	4.74	46
TiO_2 (0.5)	PVDF–HFP (MPN)	21.2	12.82	0.68	5.19	54
TiO_2 (7)	PEO:PVDF–HFP/LiI/I_2 (DMF)	7.24	6.37	0.71	2.80	63
TiO_2 (10)	PEO/KI/I_2 (MeCN)	1.35	3.71	0.76	1.68	45
TiO_2 (15)	PMII/TBP/LiI/I_2 (MeCN)	—[e]	9.00	0.61	3.74	48
SiO_2 (–)[e]	PEO/TBP/LiI/I_2 (EC:PC:MeCN)	—[e]	4.19	0.66	6.85	54
SiO_2 (2.8)	PEGDME-150/TBP/NaI/I_2	4.45	19.3	0.69	6.30	54
SiO_2 (3)	PMII/TBP/LiI/I_2 (MeCN)	—[e]	8.80	0.62	3.63	48
SiO_2 (7)	PAN:PVDF/HMII/TBP/LiI/I_2 (EC:PC)	696	11.60	0.79	5.61	53
SiO_2 (10)	PU:PPy/NaI/I_2 (PC)	2.68	3.70	0.63	2.49	57
SiO_2 (10)	PU:PANI/NaI/I_2 (PC)	2.77	3.88	0.72	3.10	57
ZnO (–)[e]	PEO/KI/I_2 (MeCN)	—[e]	2.10	0.63	1.70	56
ZnO (3)	PVDF:PEO/NaI/I_2 (EC:PC)	83.6	19.5	0.62	7.33	50
ZnO (3)	PMMA/KI/I_2 (PC)	1.84	6.05	0.61	2.38	55
ZnO (35)	PMII/TBP/LiI/I_2 (MeCN)	—[e]	9.00	0.70	4.17	48
NiO (3)	Agarose/LiI/I_2 (NMP)	33.3	6.20	0.63	2.02	67
Fe_2O_3 (7)	PAN:PVDF/ HMII/TBP/LiI/I_2 (EC:PC)	681	10.40	0.77	4.90	52
Co_3O_4 (3)	Agarose/LiI/I_2 (NMP)	42.0	3.82	0.69	1.44	70
Co_3O_4 (5)	Agarose/LiI/I_2 (NMP)	36.6	3.01	0.64	1.00	70

[a]Best performance parameters reported for TiO_2/Ru dye-based DSSCs using nanocomposite GPEs measured at room temperature. [b]Metal oxide additives commercially obtained or prepared *via* conventional hydro/solvothermal syntheses, followed by high-temperature activation. Values for wt% reflect the nanoparticle solid content loading of the GPE. [c]TBP: *tert*-butylpyridine; PVDF–HFP: poly(vinylidene fluoride-*co*-hexafluoropropylene); PMII: 1-propyl-3-methylimidazolium iodide; PEGDME: poly(ethylene glycol) dimethyl ether; PPy: polypyrrole' PANI: polyaniline. [d]NMP: *N*-methyl-1-pyrrolidinone; MPN: 3-methoxyproprionitrile; EC: ethylene carbonate; PC: propylene carbonate; MeCN: acetonitrile; DMF: *N*-dimethylformamide. [e]Data unavailable.

structural and thermochemical stability.[35–38] Yet, it is practically inactive towards ionic conductivity as a result of –CN-induced crystallization that tends to increase overall GPE resistance to ion transport.[39] Copolymerization and/or physical blending of PAN[40–43] with other polymer chains such as poly(ethylene oxide) (PEO), poly(methylmethacrylate) (PMMA), and poly(vinylace-tate) (PVAc) help to overcome its shortcomings by promoting an amorphous quasi-solid state. Indeed, the spontaneous assembly of blended and block co-polymers into a variety of nanoscale morphologies can naturally facilitate ionic conduction in PAN-based GPEs.[44] Weak binding interactions of salt additives with functional groups on the ion-conducting polymer component of these GPEs can also improve device performance by maintaining a low conduction band edge in TiO_2-based DSSCs.[18,22,26] Likewise, the introduction of nanomaterial additives such as metal oxides[45–57], mesoporous particles[58,59], nanoclays[60–62] and carbon nanomaterials[63–68] at low (e.g., <5 wt%) concentrations has been proven to augment ionic conductivity in nanocomposite GPEs, primarily through the formation of a conductive network than spans the polymer matrix. Metal oxide nanoparticles (e.g., TiO_2, ZnO, NiO, Co_3O_4, Fe_2O_3, etc.) are particularly effective at discouraging the formation of polymer crystalline domains, whilst accelerating charge transport dynamics along their surfaces. Recently, it was also shown that the addition of magnetic nanoparticle additives like Co_3O_4, Fe_3O_4 or NiO can even enable extrernal control over DSSC properties, i.e., *via* magnetic field stimuli.[69,70] In these examples, DSSC efficiencies nearly double as a result of metal oxide alignment within GPE matrixes with the magnetic field axis. See Table 1 for a summary of performance parameters for DSSCs based on GPE–oxide nanocomposites.

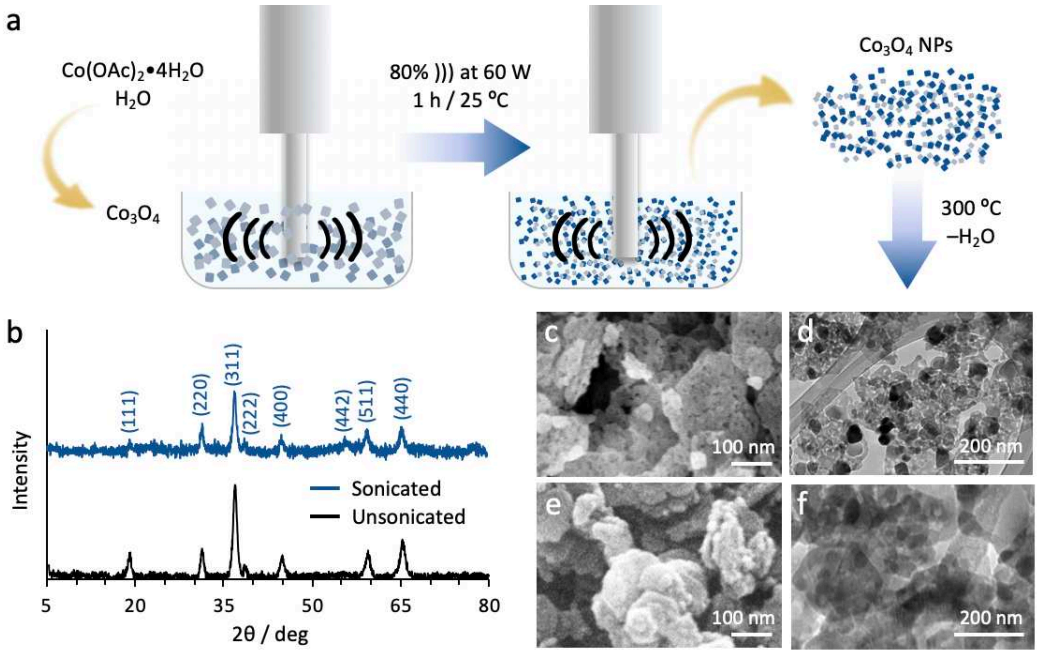

Figure 1. (a) Sonochemical processing followed by high temperature calcination at 300 °C yields a finer crop of microcrystalline Co_3O_4 nanoparticles that readily index by (b) powder XRD (λ = 1.5418 Å) to the (111), (220), (311), (222), (400), (442), (511) and (440) reflections anticipated for the cubic spinel structure of Co_3O_4 (in agreement with JCPDS Card No. 76-1802). (c) FESEM imaging of sonochemically processed and heat-treated Co_3O_4 nanoparticles reveals a flake-like porous structure caused by Ostwald ripening of individual 40 nm-sized nanocuboids. (d) HR-TEM image of sonochemically processed Co_3O_4. By comparison, (e) FESEM and (f) HR-TEM images of nanoparticles prepared without sonication form compact flakes (45–136 nm) with no apparent pore structure.

Unfortunately, such affordable metal oxide additives still come with their own limitations. Thermal activation at high temperatures (≥ 300 °C) is required to remove water (i.e., from hydrothermal syntheses), minimise hydroxide intermediates, and create good contact between fused nanoparticles for improved ionic conduction. However, this treatment also encourages particle agglomeration, thus making their uniform dispersion more difficult to achieve in GPEs. Relatively large particle agglomerates adversely affect DSSC performance[71–73] by trapping redox species and ultimately limiting the rate at which the sensitized dye can be regenerated. Resolving the aggregation of thermally activated nanoparticles is, therefore, a highly relevant task in achieving the overall mission of extending the long-term stability and performance of GPE-based DSSCs.

We identified sonochemical processing as a simple and straightforward technique that could potentially mitigate the negative effects of high temperature calcination on metal oxide nanoparticles. Acoustic cavitation has already proven to be useful for controlling particle morphologies, achieving high surface areas and inherent porosity in metal oxide materials.[74–78] This approach has also afforded carbon nanocomposite materials with high dispersity in various media.[79–81] Despite these advances, however, the technique has not been applied towards metal oxide additives in GPEs for DSSCs. We hypothesized that the use of high-power ultrasound during the solvothermal synthesis of metal oxide nanoparticles would result in finer colloids that consequently yield smaller, more easily dispersed particle agglomerates upon calcination. As a result, these sonochemically processed additives would boost the performance of GPE nanocomposite-based DSSCs.

In this work, we apply the principle of sonochemical synthesis to generate metal oxide nanoparticles that, upon annealing at 300 °C, undergo natural Oswald ripening to form relatively smaller aggregates compared to conventional (typically unsonicated) bulk metal oxides. In our experience, we have found that an annealing temperature of 300 °C is sufficiently high enough to efficiently and effectively drive off residual moisture (i.e., H_2O) trapped in and between metal oxide nanoparticles during the hydrothermal synthesis and washing steps. This condition is not dissimilar to temperatures (ranging from as low as 250 °C up to 1000 °C) applied by others to eliminate H_2O impurities.[82–85] Different wt% loadings of sonicated nanoparticles were incorporated into a PAN host matrix blended with an ion conductive poly(vinylpyrrolidone-*co*-vinylacetate)[29,81] (P(VP-*co*-VAc); 10^{-3} S cm^{-1}) and their effects on ionic conductivity and DSSC performance were measured. We have shown that when optimized, our Co_3O_4-modified GPE (i) displays an enhancement of the apparent diffusion coefficient of triioide (I_3^-) against an unmodified control GPE, (ii) raises photoconversion efficiency of DSSC devices by selectively enhancing photocurrent density, and (iii) extends their performance stability. Our results imply that a sonochemical processing strategy can broadly impact the development of composite GPEs for enhanced energy device performance.

2. EXPERIMENTAL SECTION

2.1. Materials. P(VP-*co*-VAc) (weight-average molecular weight (M_W) ~50,000 g mol^{-1} by GPC vs. PEO), vinylpyrrolidone/vinyl acetate = 1.3/1 mole ratio), PAN (M_W ~150 000 g mol^{-1} by GPC vs. PEO), cobalt(II) acetate tetrahydrate ($Co(OAc)_2•4H_2O$; 99.9% trace metal basis), NaOH,

PC (99.7%, anhydrous), EC (98%, anhydrous), poly(ethylene glycol *t*-octylphenyl ether) (Triton™ X-100, non-ionic), TiO_2 (Aeroxide® P25 (21 nm; ≥99.5%) and Aeroxide® P90 (14 nm; ≥99.5%)), and *cis*-diisothiocyanato-bis(2,2′-bipyridyl-4,4′-dicarboxylato)ruthenium(II) bis-(tetrabutylammonium) (N719; 95%) dye were used as received from Sigma-Aldrich, USA. NaI, I_2 and HNO_3 (65% *v*/*v* aqueous solution) were used as received from Friendmann Schmidt, Australia. Fluorine-doped tin oxide (FTO) conducting glass plates (sheet resistance = 8 Ω sq^{-1}; Solaronix, Switzerland) were cut into 2 × 2 cm sheets and used as substrates for the fabrication of photoanodes and platinum (Pt) counter electrodes. Tetramethylsilane (TMS) and absolute ethanol (EtOH) was used as received from Fluka, USA.

2.2. Preparation of Co_3O_4 Nanoparticles. This study took advantage of sonochemical processing, followed by calcination, to produce uniformly sized nanoparticles of cobalt oxide (Co_3O_4). A 2 M aqueous solution of NaOH (20 mL) was added dropwise to a stirring solution of $Co(OAc)_2•4H_2O$ (249 mg, 1.0 mmol) in deionized water (30 mL) under simultaneous probe ultrasonication (120 W, 60% maximum amplitude; Fisher Scientific, USA). Afterwards, the resulting blue-green solution was probe sonicated for 1 h, during which time a maximum internal temperature of 60 ± 5 °C was recorded and a fine black precipitate was formed. The colloidal mixture was spun down by centrifugation (6000 rpm for 15 min; Hettich, Germany), the supernatant decanted, and the particles re-suspended in deionized water (12 mL). This washing protocol was repeated several times (*ca.* 5–6 times) until the supernatant was observed to be colorless. After removal of the supernatant, the solid was dried in an oven at 90 °C for 8 h before being ground into a fine powder by mortar and pestle and calcined in an electric muffle furnace (JS Research Inc., Korea) under air at 300 °C for 3 h to afford activated Co_3O_4 nanoparticles with an average particle size of 40.9 ± 0.3 nm. See *Supporting Information* for details on the preparation unsonicated Co_3O_4 nanoparticles.

The surface morphology of as-prepared Co_3O_4 nanoparticles were examined using field emission scanning electron microscopy (FESEM; JEOL JSM-7600F, Japan) and high-resolution transmission electron microscopy (HR-TEM; Hitachi-7100, Japan). Structural crystallinity and phase purity were confirmed by powder X-ray diffraction (XRD) analysis using a Empyrean X-ray diffractometer (PANalytical, USA) at 25 °C with Cu Kα radiation (45 kV, 40 mA; λ = 1.5418 Å) in the 2θ range from 5° to 80° at 0.1° step intervals and a 10 s count time.

2.3. Preparation of Co_3O_4-Modified GPEs. The GPEs investigated in this study were prepared using a 'PVVA' electrolyte formulation preiously reported by us[81,86] that has been optimized with respect to the NaI/I_2 redox couple (see the *Supporting Information* for further details.) Varying amounts of either sonicated or unsonicated Co_3O_4 nanoparticles (i.e., 0, 1, 3, or 5 wt% Co_3O_4 with respect to total solid contents) were added to a 1:1 *w*/*w* (2 g) PC:EC solvent mixture containing a 10:1 *w*/*w* ratio (200 mg) of the $NaI:I_2$ redox couple. The black suspension was sonicated while stirring for 30 min to ensure the complete and uniform dispersion of Co_3O_4 before finally adding a 1:1 *w*/*w* blend (300 mg) of PVP-*co*-PVAc and PAN. The resulting mixture was stirred at 100 °C until the polymer components were fully dissolved, then cooled back down to room temperature, triggering gelation. The resulting GPEs were used directly in electrochemical studies and DSSC fabrication without additional treatment.

The extent of GPE crystallinity was determined using powder XRD analysis, while complexation of the polymer matrix was investigated by absorbance-mode Fourier transform infrared (FTIR) spectroscopy on a Nicolet™ iS10 FTIR spectrometer (Thermo Fisher Scientific, USA) equipped with a Smart iTR™ accessory. Solid-state cross-polarized magic angle spinning (CPMAS) nuclear magnetic resonance (NMR) spectra were recorded using a 400 MHz Bruker Avance III HD SS-NMR spectrometer (Germany) at 25 °C. GPE films were cut into approximately 1.0 mm^2 pieces using a clean razor blade and packed into a 4 mm (⌀) CPMAS rotor. These NMR samples were then spun at 54.71° (the 'magic angle') at a spin rate of 10 Hz. ^{13}C CPMAS NMR spectra were obtained at frequencies of 100.63 MHz, respectively, using a 1 ms contact time and 2 s recycle delay and referenced with respect to neat TMS (δ_C = 0 ppm) by setting the high-frequency signal of adamantane to a δ_C of 38.5 ppm. ^{23}Na CPMAS NMR spectra were recorded at a frequency of 105.85 MHz using direct excitation with a 0.1 s recycle delay and referenced with respect to a 1 M aqueous solution of NaCl (δ_{Na} = 0 ppm).

Ionic conductivities of the GPEs were determined by electrochemical impedance spectroscopy (EIS; HIOKI LCR Hi-Tester Model 3532-50, Japan) at 25 °C at an AC voltage of 10 mA within a frequency range of 50 Hz to 5 MHz. GPE samples were sandwiched between two stainless steel blocking electrodes (hole area, S = 2.0 cm^2) to a thickness, l, of 2.9 mm. Temperature-dependent EIS measurements were carried out on GPE samples from 30 to 100 °C in 10 °C intervals. The effective diffusion coefficient of triiodide ions ($D_{app}^{I_3^-}$) in GPEs was determined by carrying out steady-state linear-sweep voltammetry (LSV) experiments with a potentiostat (PGSTAT-128N; Metrohm Autolab, The Netherlands) at a scan rate of 10 mV s^{-1} between ±700 mV at 25 °C. The dummy cell used in LSV studies consisted of GPE samples sandwiched between two Pt counter electrodes (hole area, S = 0.2 cm^2) in a Pt|GPE|Pt configuration with a spacer thickness, l, of 48 μm.

2.4. DSSC Fabrication and Characterization. See *Supporting Information* for details on preparing the TiO_2 photoanode. DSSCs were fabricated by sandwiching the desired GPE sample between a 12 μm-thick TiO_2 photoanode (0.10 cm^2 active area) and a Pt counter electrode. The height of the GPE layer was controlled using a spacer of 48 μm thickness. Photovoltaic DSSC performance and current density–voltage (*J*–*V*) curves were measured using a 'Class A' quality solar simulator (AM1.5G, Xe lamp; Newport LCS-100 Series, USA) coupled to a potentiostat. EIS data of fabricated DSSCs were recorded between 0.1 Hz and 100 kHz at an open-circuit AC potential of 10 mV using a frequency response analyzer (Metrohm Autolab, The Netherlands) and fitted to an equivalent circuit model using the Metrohm Autloab Nova software. EIS data was recorded under illumination at an applied bias of 0.55 V and 10 mV s^{-1} scan rate. The illumination intensity

(100 mW cm^{-2}) used in all DSSC measurements was calibrated with a solar power meter (TENMARS TM-207; Taiwan) using a standard Si cell. The active area of DSSC devices was fixed to 0.10 cm^2.

3. RESULTS AND DISCUSSION

3.1. Sonochemically Synthesized Co_3O_4 Nanoparticles. We originally envisioned that the addition of well-defined porous Co_3O_4 nanoparticles would encourage fast ion diffusion and conductivity in GPE-based DSSCs by enhancing interactions in the GPE matrix and yielding lower-energy charge-transport pathways. Sonochemical processing, followed by calcination under air at 300 °C for three hours, proved to be an excellent method for achieving the reliable synthesis of crystalline nanoporous Co_3O_4 nanocubes (Figure 1a). Powder XRD analysis of sonicated and unsonicated Co_3O_4 nanoparticles post-calcination display similar sets of diffraction peaks located at 19.1, 31.5, 36.9, 38.6, 44.9, 55.8, 59.6 and 65.5° 2θ that clearly index (Figure 1b) to the reflections of a face-centered cubic spinel structure for bulk crystalline Co_3O_4, in agreement with standard (JCPDS No. 76-1802) values. Considering the FWHM of the powder diffraction peaks, the average crystallite size of the sonicated and unsonicated Co_3O_4 nanoparticles can be calculated using Scherrer's formula[87,88]:

$$B_{2\theta max} = K\lambda \,/\, \beta\cos\theta \qquad (1)$$

where K is unitless Scherrer or shape constant, λ is the diffraction wavelength (= 1.5418 Å), and β is the FWHM at angle 2θ in radians. K is assumed to be 0.94 for the FWHM of a crystal with cubic symmetry. By this method, sonicated Co_3O_4 nanoparticles in this study are found to possess smaller crystallite sizes (ca. 10.2 nm) compared to Co_3O_4 nanoparticles prepared without sonication (ca. 11.7 nm). These calculations imply that the applied acoustic cavitation was effective at limiting the size of metal oxide nanoparticles and agglomerates post-calcination. Comparing the powder XRD pattern of bulk Co_3O_4 with that of the sonicated Co_3O_4 nanoparticles, we can see that the latter appears slightly broadened, which can be attributed to the mechanical tension associated with the high-heat extraction of solvent from the particle surface. Even so, the effect of thermal annealing on the overall crystallinity of Co_3O_4 nanoparticles appears to be negligible.

Electron micrographs of sonicated Co_3O_4 (Figures 1c–f) reveal that the calcination step is critical for fusing sonicated Co_3O_4 nanoparticles into a porous network morphology. FESEM images (Figure 1c of drop-cast aliquots show the porous flake-like structure of annealed Co_3O_4 nanoparticles that appear to be composed of smaller Co_3O_4 nanocuboids (40.9 ± 0.3 nm). HR-TEM images (Figure 1d) of the Co_3O_4 nanoparticles further illustrate the cuboidal shapes observed by FESEM. Compared to other sonochemically prepared metal oxides reported in the literature,[72–76] the nanocuboids obtained *via* sonochemical processing occupy a rather narrow size distribution. In contrast, FESEM and HR-TEM images of the unsonicated Co_3O_4 (Figures 1e,f) show densly compacted nanoparticles with no apparent porous structure. Indeed, Brunauer–Emmett–Teller (BET) surface area analysis of the two samples (see Supporting Information, Figure S1) reveals N_2 adsorption–desorption isotherms with a Type IV hysteresis between P/P_0 = 0.9 and 1, indicating their mesoporous natures. We determined BET surface areas of 80.909 and 65.168 m^2/g for the sonicated and unsonicated Co_3O_4 nanoparticles, respectively, thus providing evidence of enhanced surface area and total pore volume as a result of sonochemical processing. We surmise that the higher surface area nanoparticles will display excellent dispersion and contact with the polymer matrix to facilitate ion transport within GPEs.

3.2. Co_3O_4-Modified GPEs. We prepared GPE samples PVVA, PVVA-1, PVVA-3, and PVVA-5 consisting of 0, 1, 3, 5 wt% of sonicated Co_3O_4 solid content, respectively. Please see the *Experimental Section* and *Supporting Information* for further details on GPE optimization. GPE samples consisted of Co_3O_4 nanoparticles dispersed in a matrix containing a 50:50 ratio of a 1:1 *w*/*w* PAN:P(VP-*co*-VAc) blend and the NaI/I_2 redox couple along with PC and EC as small molecule plasticizers. Room temperature gelation of the viscous mixtures resulted afforded GPEs (Figure 2a) that were pliable yet mechanically robust thanks to the structural stability offered by the PAN component. Increasing the sonicated Co_3O_4 content beyond 5 wt% was found to impede gelation, presumably due to a higher concentration of nanoparticle aggregates interfering with the association of polymer chains needed to achieve a stable quasi-solid state.

Brief inspection of the FTIR spectra (Figures S2) reveals particularly strong stretching frequencies associated with the PC and EC plasticizers for all GPE samples. A notable shift (Figure S3) in the diagnostic lactam C=O stretch of the P(VP-*co*-VAc) component from 1680 cm^{-1} in the pure polymer to between 1657 and 1669 cm^{-1} for GPEs is indicative of their increased *lp* interactions within the host polymer matrix. Indeed, *N*-tertiary pyrrolidinones such as P(VP-*co*-VAc) have a propensity to form diverse multivalent complexes with alkali metal cations, even resulting in linear coordination polymers.[89] Relative to PVVA, bathochromic shifts of the GPE lactam C=O stretches suggest that metal complexation is taking place, i.e., through an amide –O···Na^+ interaction. Minor variations in the position of the C=O stretch may indicate the relative strength of cation–*lp* interaction taking place as a function of Co_3O_4 nanoparticle loading. Line broadening effects observed by solid-state ^{23}Na CPMAS NMR spectroscopy performed on GPE samples (Figures S4 and S5) also support the notion weak complexes are formed between Na^+ and pendant lactam/ester carbonyl groups of the P(VP-*co*-VAc) component. These dynamic interactions are anticipated to lower the activation barrier for ion transport to occur.

Powder XRD analysis (Figure 2b) of Co_3O_4-modified GPEs more clearly reveals the impact of sonicated nanoparticles on polymer chain interactions in the quasi-solid state. The PVVA matrix is characterized by a single broad diffraction peak spanning 25° and centered at 2θ = 30.8°, confirming its highly amorphous nature. Powder XRD spectra of the sonicated Co_3O_4-modified GPEs PVVA-1, PVVA-3 and PVVA-5 display relatively narrowed diffraction signals situated at lower angles of 2θ (maxima centered around 22.4°, 28.4° and 25.9°, respectively) relative to PVVA. This trend towards lower angles of 2θ results from an increase in the interlayer spacing d (i.e., of Bragg's relation)

between (micro)ordered polymer chains within the matrix, which would be consistent with the intercalation of nanoparticle additives. Increasing the solid content of sonicated Co_3O_4 nanoparticles from 1 wt% to 3 wt% (i.e., PVVA-3) reduces the degree of crystallinity in GPEs, as evidenced by broadening of the overall peak area centered at 2θ = 28.4° and a reduction main peak intensity. Conversely, raising the solid content of sonicated Co_3O_4 to 5 wt% in PVVA-5 seems to re-establish the main peak area and intensity, suggesting that nanoparticles coalesce to form more crystalline domains within the GPE matrix at (and above) this concentation threshold. On the whole, these data reveal that the introduction of 3 wt% sonicated Co_3O_4 to PVVA-based GPEs achieves a 'sweet spot' with respect to (i) retaining the most amorphous GPE phase whilst (ii) reducing the distance between polymer chains (i.e., d = 3.14 Å) to overall enhance ion transport and mobility in the matrix. Comparison with the homologous GPE consisting of 3 wt% *unsonicated* Co_3O_4 nanoparticles (Figure 2c) reveals a relatively sharper peak at 21.5° 2θ, highlighting the role of sonochemical processing to avoid the formation of higher crystalline matrixes.

FESEM micrographs taken of the homologous GPE films (Figure S6) reveal that sonochemical processing leads to finer Co_3O_4 nanoparticles dispersions and a more uniform polymer matrix in PVVA-3, whereas crystallite domains can be clearly identified in the FESEM image of the film containing Unsonicated nanoparticles Such bridging interactions between nanoparticles and the host matrix are thought to encourage cooperative ion complexation along the polymer backbones in order to achieve more efficient charge transport in the solid state. From these initial data,

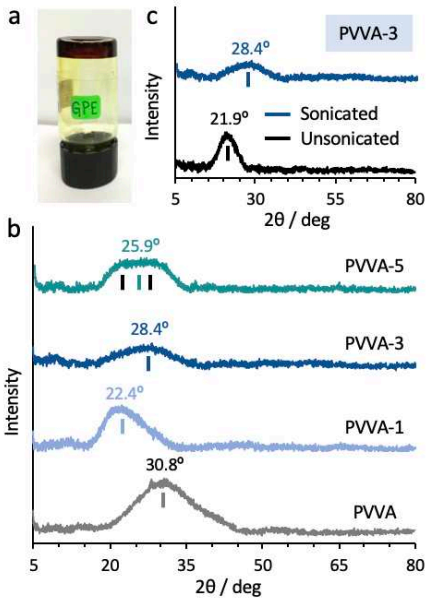

Figure 2. (a) A typical GPE used in this study. (b) Powder X-ray diffraction analysis of GPEs consisting of 0, 1, 3, 5 wt% of sonicated Co_3O_4 (i.e., PVVA, PVVA-1, PVVA-3, and PVVA-5, respectively) reveals that a 3 wt% loading provides an optimum balance of low matrix crystalline phase and close interlayer spacing (d = 3.14 Å) between polymer chains. On the other hand, (c) a homologous control GPE of PVVA-3 bearing 3 wt% of *unsonicated* Co_3O_4 nanoparticles displays relatively larger distances within a more crystalline polymer matrix.

it is clear that balancing nanoparticle loading against the amorphousness of the solid-state is a non-trivial but critical task for optimizing GPEs for DSSC development.

3.3. Electrochemical Performance of GPEs. AC electrochemical impedance analyses (Figure 3) was used to investigate the ionic conductivity of GPEs as a function of Co_3O_4 content and processing. Co_3O_4-modified GPEs were sandwiched between two stainless steel blocking electrodes (hole area, S = 2.0 cm^2; spacer thickness, l = 2.9 mm) and evaluated against the control GPE (PVVA). The ionic conductivities (σ) of the GPEs were determined by the following equation:

$$\sigma = R_I^{-1} S^{-1} l = R_B^{-1} S^{-1} \quad (2)$$

where R_I is the real-axis intercept of impedance spectra from the Nyquist plot, S is the geometric surface area of the GPE-electrode interface, and l is the distance between the two electrodes.

Room temperature impedance spectra as well as variable temperature data between 30 and 100 °C (Figures 3a, S7 and S8) show all three sonicated Co_3O_4-modified GPEs delivering real-component impedance (Z') values smaller than PVVA. These data confirm that Co_3O_4-modified GPEs must be more efficient in facilitating ion transport through the host polymer matrix, where the following values for σ were obtained at 25 °C: 3.89 × 10^{-3} (PVVA-1), 4.62 × 10^{-3} (PVVA-3), 3.93 × 10^{-3} (PVVA-5), 3.97 × 10^{-3} (PVVA-3 unsonicated) and 3.57 × 10^{-3} S cm^{-1} (PVVA). A summary of these ionic conductivities and related values obtained from EIS measurements can also be found in Table 2. Indeed, the phase-optimized PVVA-3 displayed the lowest bulk resistance ($R_B = R_I^{-1} d$ = 31.7 Ω) and highest ion conductivity overall. The Nyquist data satisfyingly follow the trend in electrochemical performance (i.e., PVVA-3 > PVVA-5 > PVVA-1) anticipated from powder XRD analyses (*vide supra*). Beyond a certain critical wt% threshold,[71] the formation tendency of larger crystalline aggregates begins to hinder charge transport efficiencies by raising the percolation threshold of redox species between ion-conducting polymer chains. Here, it is evident that a solid content loading of Co_3O_4 beyond 3 wt% does not lead to more favourable charge mobilities.

Temperature-dependent ionic conductivity measurements taken between 30 and 100 °C provided us with further insight into the ion transport mechanism taking place in Co_3O_4-modified GPEs. Arrhenius plots (Figure 3b) show the log(σ) of GPEs with respect to inverse temperature plotted as 1000/T. Here, changes in ionic conductivity are observed to be linearly dependent. Their ionic conductivity behavior can thus be expressed by the Arrhenius[90] equation:

$$\sigma = \sigma_0 \exp(-E_a / k_B T) \quad (3)$$

in which σ_0 is the pre-exponential frequency factor, E_a is the activation energy, k_B is Boltzmann's constant, and T is absolute temperature. Such a profile suggests that Co_3O_4-modified GPEs are homogenous (as far as ion mobility phase is concerned) with no large polymer chain rearrangements taking place as the temperature is increased.

In other words, general diffusion and conductive behaviour of charge carriers in our GPE design can be described

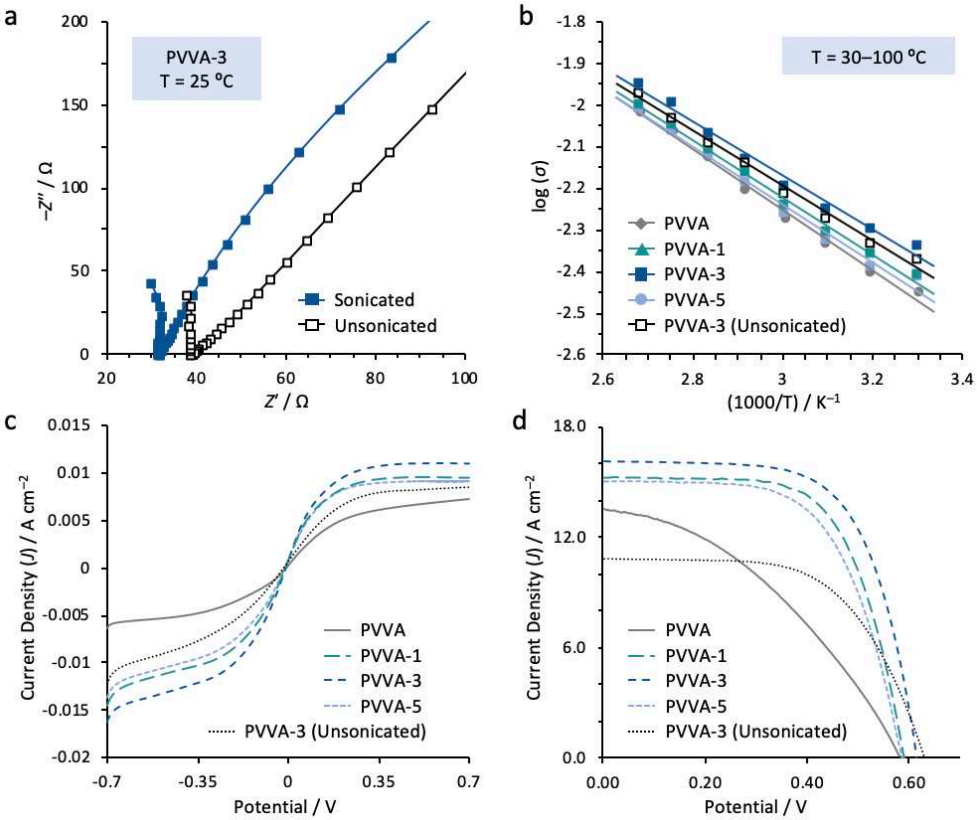

Figure 3. (a) Room temperature impedance spectra reveal a marked increase in resistance towards ion mobility for the sonochemically enhanced GPE PVVA-3 versus its homologue containing 3 wt% unsonicated Co_3O_4 nanoparticles, evidenced by a lower Z' intercept. The linear relationship between log(σ) and inverse temperature in the (b) Arrhenius plots are indicative of a charge-hopping ion transport mechanism within the GPEs. (c) Linear sweep voltammograms taken at room temperature reveal an 51% enhancement in the apparent diffusion coefficient of triiodide species ($D_{app}^{I_3^-}$) within the optimized PVVA-3 sample versus PVVA and its unsonicated homologue. (d) *J–V* curves of Co_3O_4-modified DSSCs show enhanced photovoltaic performance over an unmodified cell, where the device containing PVVA-3 outperforms all other devices in the study. DSSCs were operated under AM1.5G at an illumination intensity of 100 mW cm^{-2}.

Table 2. Electrochemical Impedance-Derived Properties of GPEs

GPE	wt% Co_3O_4	R_B / Ω	σ^a /10^{-3} S cm^{-1}	$E_a{}^b$ / eV	$D_{app}^{I_3^-}$ / 10^{-8} cm^2 s^{-1}
PVVA	0	40.5	3.57	0.144	2.19
PVVA-1	1	37.2	3.89	0.137	2.71
PVVA-3	3	31.3	4.62	0.128	3.30
PVVA-5	5	36.8	3.93	0.136	2.81
PVVA-3 Unsonicated	3	36.5	3.97	0.131	2.51

[a]Ionic conductivity at 25 °C. [b]Activation energy determined from the Arrhenius plot (equation 3)

as hopping to nearest and energetically favorable vacant (e.g., empty, interstitial, and (sub)lattice) sites[91] throughout the host polymer framework.

This model is unlike other common ion transport mechanisms reported in the literature, such as that described by the Vogel–Thammann–Fulcher[92–94] model where charge carrier diffusion instead arises from the molecular motion of the polymer chains at greater temperatures to generate free volume within the host matrix. Even at higher temperatures, the Arrhenius behaviour of our GPEs is preserved, demonstrating the structural contributions of a PAN blend to limit segmental motion[91,95,96] of polymer chains within the host matrix. With respect to E_a, Co_3O_4-modified GPEs display lowered activiation energies in comparison to unmodified PVVA. These variations suggest that a homogenous dispersion of fine Co_3O_4 nanoparticles can aid the formation of interstitial lattice sites between polymer chains which in turn facilitate ion hopping through the quasi-solid-state. The rise in E_a from PVVA-3 to PVVA-5 can be attributed to the fact that higher weight percentages of Co_3O_4 nanoparticles can lead to the formation of larger nanocrystalline aggregates, which ultimately cane impede ion diffusion by disrupting access of ions to the vacant sites of the host lattice.

The results of linear sweep voltammetry (LSV) experiments (Figure 3c; Table 2) carried out on Co_3O_4-modified

GPEs to determine the effective diffusion coefficient of triiodide ions ($D_{app}^{I_3^-}$) stand in agreement with our EIS analyses. Based on the known mechanism of dye-sensitized photovoltaics, the $D_{app}^{I_3^-}$ of this key rate-determining species could be determined by the following equation:

$$D_{app}^{I_3^-} = J_{\text{lim}}\left(\frac{l}{2nFC}\right) \quad (4)$$

where J_{lim} is the steady-state photocurrent density, l is the GPE thickness, n is the number of electrons (i.e., n = 2), F is the Faraday constant and C is the concentration of I_3^- ions. Here, J_{lim} is maximized at 0.011 mA cm^{-2} in PVVA-3. Moreover, PVVA-3 achieves the greatest enhancement in $D_{app}^{I_3^-}$, going from 2.19 × 10^{-8} cm^2 s^{-1} for PVVA to a value of 3.30 × 10^{-8} cm^2 s^{-1}. This 51% overall enhancement in effective ion diffusion is consistent with our observation of a highly amorphous matrix offered by an optimized 3 wt% loading of sonicated Co_3O_4. Notably, a literature survey of diffusion coefficients for GPEs augmented with other conventionally obtained and/or untreated metal oxides reveals $D_{app}^{I_3^-}$ values to typically span a 10^{-6} to 10^{-10} cm^2 s^{-1} range,[48,55,63] calling attention to the general advantage provided by sonochemical processing for improving the performance of GPE nanocomposites.

3.4. GPE Performance in DSSCs. Lab-scale DSSC devices were fabricated by sandwiching an N719-sensitized TiO_2 mesoporous anode with the prepared GPEs and a Pt counter electrode between two transparent FTO substrates. *J–V* curves of the as-prepared DSSCs were measured and are provided in Figure 3d above. From Table 3 below—which summarizes the short-circuit photocurrent (J_{SC}), open circuit potential (V_{OC}), fill factor (*FF*) and photovoltaic conversion efficiency (PCE; η)—it is clear that device J_{SC} values are sensitive and positively influenced by sonochemically processed Co_3O_4 nanoparticles in the PVVA host matrix—up to 16.2 mA cm^{-2} in PVVA-3. On the other hand, the presence of 3 wt% unsonicated nanoparticles appears to have a detrimental effect on the J_{SC} value (11.5 mA cm^{-2}), though the device efficiency is still better than the one containing unmodified PVVA electrolyte.

Given that our DSSCs were constructed and measured under consistent temperatures and device components, increases in J_{SC} cannot be attributed to either thermal acceleration of ions in the GPE or differences in photoanode characteristics. On the other hand, improved dye regeneration kinetics, which are ultimately influenced by the efficiency of ion diffusion and charge transport within the electrolyte layer, can lead to increased J_{SC} values. In this vein, the apparent rise in J_{SC} here can be reasonably attributed to ion diffusion of the redox-active species across a bridged nanoparticle network, made more made more effective as a result of sonichemical processing, *via* a Grotthus-type electron hopping–ion exchange mechanism, i.e.,

$$I^- + I_3^- \rightleftharpoons I^-—I_2\cdots I^- \rightleftharpoons I^-\cdots I_2—I^- \rightleftharpoons I_3^- + I^- \quad (5)$$

Previous reports[95,96] have shown that iodide exchange processes occur in viscous/gel electrolyte media to afford the adsorption of redox-active species at the nanoparticle surface. The formation of dense, highly oriented regions enables rapid I_3^- transport with little to no physical species transfer observed. This mechanism bears similarity to the chemical bond exchange processes that enables proton transport in aqueous media.[97,98] We surmise that sonochemically prepared nanoparticles may act in a similar capacity, i.e., as potential redox mediators for dye regeneration. By lessening the degree of aggregation that is inherently caused by thermal annealing with sonochemical processing, the relatively high surface area of the nanoparticles can be retained. This, as well as the internal pore structure generated by acoustic cavitation, enable the alignment of a local density of I^-/I_3^- to accelerate redox couple diffusion along a bridged particle network[99] in GPEs. It is this re-sensitization of the TiO_2 photoanode by mobilization of the charge carriers that ultimately accounts for the observed increases in J_{SC}, *FF*, and PCE.

We were pleased in the end to find that the device based on PVVA-3—our best performing GPE—also delivers the best PCE (η) of 6.46%. This result represents a more than two-fold improvement over the DSSC lacking any additive as well as a more than four-fold efficiency enhancement over a recent previous report.[70] To the best of our knowledge, our work represents the highest PCE reported for Co_3O_4-modified GPEs of either homo-, co- or blended polymer host compositions (Table 1.)

EIS analysis via Nyquist plots (Figure 4) of our devices helped us gain a more complete understanding of which interfacial processes may be influenced by the presence of sonochemically processed Co_3O_4 nanoparticles. The equivalent circuit model of our devices is given in the inset

Table 3. Photovoltaic Performance and Equivalent Circuit Parameters Fitted to EIS Data of DSSCs

DSSC[a]	J_{SC} / mA cm^{-2}	V_{OC} / V	*FF* / %	η / %	R_S / Ω	R_{PT} / Ω	R_{CT} / Ω
PVVA	13.5 ± 0.3	0.590 ± 0.01	0.383 ± 0.01	2.96 ± 0.09	40.4 ± 0.10	10.50 ± 0.05	92.2 ± 0.50
PVVA-1	15.1 ± 0.2	0.580 ± 0.01	0.616 ± 0.01	5.33 ± 0.10	32.0 ± 0.20	49.4 ± 0.10	157.0 ± 0.50
PVVA-3	16.2 ± 0.1	0.610 ± 0.01	0.657 ± 0.01	6.46 ± 0.10	20.70 ± 0.05	41.60 ± 0.09	193.0 ± 0.10
PVVA-5	15.3 ± 0.2	0.580 ± 0.01	0.640 ± 0.01	5.78 ± 0.09	25.20 ± 0.06	41.30 ± 0.04	180 ± 0.20
PVVA-3 unsonicated	11.5 ± 0.4	0.620 ± 0.01	0.58 ± 0.01	3.99 ± 0.04	18.80 ± 0.05	10.90 ± 0.05	95 ± 0.10

[a]Data is measured and averaged for three devices.

of Figure 4. Two distinct semi-circle profiles are detected at low (0.1–10 Hz) and high (10–10^5 Hz) frequencies, representing the occurrence of charge recombination phenomena (R_{CT}) and charge transfer processes at the Pt|GPE interface (R_{Pt}), respectively. The intersection at the *x*-axis is interpreted as ohmic serial resistance[100] (R_S) of the as-prepared FTO substrate. We found that the total impedance of the sonochemically enhanced DSSCs is dominated by a high charge-transfer resistance (R_{CT} ranging between 60 and 250 Ω), meaning that the tendency of electrons to recombine with I^-/I_3^- ions in GPEs has been significantly reduced in the presence of processed nanoparticles. Interaction of the oxidized redox species with the surface and internal pore structure of the Co_3O_4 nanoparticles are likely to mitigate the back reaction of electrons within the TiO_2 conduction band, therefore extending the effective lifetime and overall performance of the present DSSC devices. This argument stands in agreement with EIS data collected for the DSSC comprised of unmodified PVVA: a

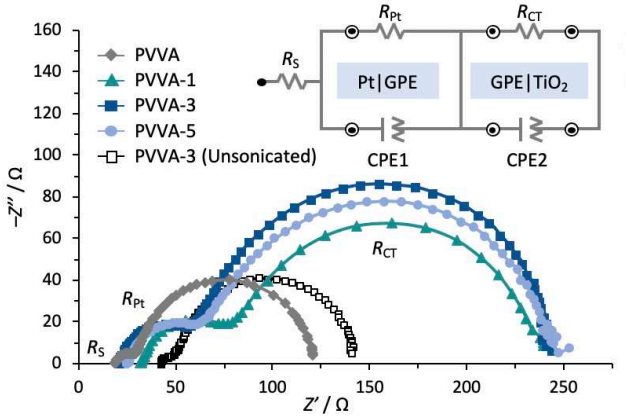

Figure 4. Electrochemical impedance data collected for GPE-based DSSCs show that sonochemically processed Co_3O_4 additives confer higher resistance (R_{CT}) towards charge recombination events (i.e., of I_3^-) in GPEs, thus enabling fast N719 dye regeneration for enhanced DSSC performance. *Inset:* An equivalent circuit model has been fitted to the EIS data.

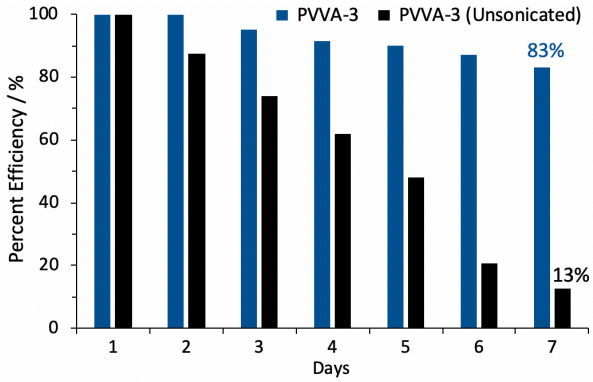

Figure 5. Photovoltaic performance stability of DSSCs employing Co_3O_4-modified GPEs, plotted as percent efficiency over time. The sonochemically enhanced DSSC consisting of the GPE PVVA-3 retains 83% of its initial efficiency over the course of seven days, whereas the untreated cell is found to experience an 87% efficiency loss in the same period.

resistance to iodide charge. From these results, the apparent increases in J_{SC} and PCE can be clearly attributed to the ability of sonochemically processed Co_3O_4 additives to substantially mediate the charge-transfer dynamics of redox couples in the PVVA gel state.

3.5. Stability of DSSCs Bearing Co_3O_4-modified GPEs.

Finally, given the importance of addressing device stability in additional to enhanced efficiencies, we sought out to interrogate the relationship between our Co_3O_4 processing method and DSSC performance over time. The performance of our best DSSC (PVVA-3) was monitored over seven days and compared to the homologous device containing 3 wt% unsonicated Co_3O_4 nanoparticles. Both devices were stored at room temperature and under ambient conditions between each test. Plotting the normalized efficiencies over time (Figure 5) revealed a dramatic loss in DSSC performance for the device employing unsonicated nanoparticles. Compared to that of the DSSC based on PVVA-3, which retained at least 83% of its initial efficiency, the unsonicated cell only retained 13% efficiency after seven days. We suspect this remarkable retention in DSSC performance for sonochemically enhanced PVVA-3 has to do with the finer porous structure and higher surface area of the nanoparticle network slowing down cell degradation and GPE collapse caused by the evaporation of carbonate solvent molecules from the matrix. Thus, on top of improving overall device performance parameters, we find rather serendipitously that the sonochemical process has the potential to extend the performance integrity and stability of quasi-solid-state devices.

4. SUMMARY AND CONCLUSIONS.

We have successfully applied a sonochemical processing method to access nanoporous Co_3O_4 particles that display relatively high dispersibilities and surface areas to promote faster ion transport within GPEs for enhanced quasi-solid-state DSSC performance. FESEM and HR-TEM analysis of the annealed metal oxide reveal the formation of porous flakes composed of individual nanocuboids, in agreement with the powder XRD data. The high dispersibility of sonicated Co_3O_4 nanoparticles (1, 3, and 5 wt% solid content) in a PVVA polymer-blended host matrix resulted in homogenous quasi-solid-state GPEs with highly amorphous phases. A GPE modified with 3 wt% sonicated Co_3O_4 nanoparticles (PVVA-3) was found to be the best performing GPE in our series, providing an ionic conductivity and apparent diffusion coefficient value of 4.62 x10^3 S cm^{-1} and 3.30 x10^{-8} cm^2 s^{-1}, respectively. The latter value represents a 51% enhancement in triiodide diffusion kinetics over an unmodified PVVA-derived GPE lacking any nanoparticle content, which we attribute to an interconnected particle network for contiguous ion transport. These attributes translated to a maximum photovoltaic conversion efficiency, η, of 6.46% in quasi-solid-state DSSCs—the highest known efficiency to-date for a Co_3O_4-modified GPE-based cell. Electrochemical impedance analysis of DSSCs have revealed that the addition of Co_3O_4 nanoparticles selectively enhance the photocurrent density (J_{SC}) and

rate of dye regeneration *via* a high recombination charge transfer resistance (R_{CT}). The GPE containing a higher weight percent content of sonicated Co_3O_4 (i.e., PVVA-5) led to reduced DSSC efficiency (η = 5.85%) on account of more crystalline particle deposits present within the GPE matrix. Likewise, the homologous GPE of PVVA-3 containing unsonicated Co_3O_4 nanoparticles showed a lowered photovoltaic conversion efficiency of 3.99%, further attributing the improvement in DSSC performance to the sonochemical process. Finally, the use of sonochemically processed nanoparticles was found to extend the performance stability of DSSCs with an overall 83% retention in device efficiency (versus 13% in the homologous untreated cell) after one week of monitoring.

Our studies demonstrate the importance in balancing optimizing metal oxide content with device performance. By comparing our sonochemically enchanced photovoltaic device to similar devices reported prior, especially that employing equivalent quantities of conventionally obtained Co_3O_4, it appears that including a sonochemical processing step can lead to a greater than two-fold increase in DSSC performance. Moreover, sonochemically prepared Co_3O_4 nanoparticles may yet reveal further enhanced properties in DSSCs when subjected to a magnetic field versus their bulk analogues. We are hopeful that such a straightforward and generally applicable technique will allow stable quasi-solid-state DSSCs based on low-cost metal oxides to reach performance levels that are meaningful for real-world exploitation.

ASSOCIATED CONTENT

Supporting Information

Details on the preparation of unsonicated Co_3O_4 nanoparticles; GPE optimization notes; details of photoanode fabrication; FTIR data; solid-state CPMAS NMR spectra; electrochemical impedance data of PVVA, PVVA-1, PVVA-3 and PVVA-5 at varying temperatures. The Supporting Information is available free of charge on the ACS Publications website at http://pubs.acs.org.

AUTHOR INFORMATION

Corresponding Authors

*E-mail: ramesh@um.edu.my
*E-mail: alyssa-jennifer.avestro@york.ac.uk

AUTHOR CONTRIBUTIONS

Nanoparticle synthesis, gel polymer electrolyte processing and electrochemical experiments were performed by N.M.S., F.S.O., and A.N. Solid-state NMR analysis was provided by D.C.A. Materials imaging analysis was completed by M.M.A. The research was designed by R.T.S. and A.-J.A. with intellectual contributions from R.K. The manuscript was written through the contributions of all authors, with final figures and editing performed by A.-J.A. and R.T.S. All authors have given approval to the final version of the manuscript.

Notes

The authors declare no competing financial interest.

ACKNOWLEDGMENT

The authors would like to thank Collaborative Research in Engineering, Science & Technology Center (CREST) for their continuous support in this research (PV027-2018). A special thank you to ECLIMO SDN BHD as well. S.R. gratefully acknowledges the Institute of Advance Studies at Durham University for the award of a Durham International Fellowship for Research and Enterprise (DIFeREns2) Senior Research Fellowship, a project of the European Union's Seventh Framework Programme, to carry out part of this collaborative work in the United Kingdom in collaboration with A.-J.A., D.C.A, and M.M.A. A.-J.A. thanks the Royal Commission for the Exhibition of 1851 for the award of a 1851 Research Fellowship in Science and Engineering, which provided her research funding support while at Durham University. A.-J.A. would also like to thank the Royal Society and the Global Challenges Research Fund for the recent award of a jointly-funded five-year Royal Society Dorothy Hodgkin Fellowship (DHF\R1\180106), which has allowed her to continue this work at the University of York. M.M.A. acknowledges the King Khalid Military Academy for funding his sabbatical at Durham University to engage in this research project.

REFERENCES

(1) O'Regan, B.; Grätzel, M. A Low-Cost, High-Efficiency Solar Cell Based on Dye-Sensitized Colloidal TiO_2 Films. *Nature* **1991**, *353*, 737–740.

(2) Green, M. A.; Hishikawa, Y.; Warta, W.; Dunlop, E. D.; Levi, D. H.; Hohl-Ebinger, J.; Ho-Baillie, A. W. H. Solar Cell Efficiency Tables (Version 50). *Prog. Photovoltaics* **2017**, *25*, 668– 676.

(3) Hardin, B. E.; Snaith, H. J.; McGehee, M. D. The Renaissance of Dye-Sensitized Solar Cells. *Nature Photonics*, **2012**, *6*, 162–169.

(4) Theerthagiri, J.; Senthil, A. R.; Madhavan, J.; Maiyalagan, T. Recent Progress in Non-Platinum Counter Electrode Materials for Dye-sensitized Solar Cells. *ChemElectroChem* **2015**, *2*, 928-945.

(5) Theerthagiri, J.; Senthil, R. A.; Buraidah, M. H.; Madhavan, J.; Arof, A. K.; Ashokkumar, M. One-step Electrochemical Deposition of $Ni_{1-x}Mo_xS$ Ternary Sulfides as an Efficient Counter Electrode for Dye-sensitized Solar Cells. *J. Mater. Chem. A* **2016**, *4*, 16119–16127.

(6) Yu, Z.; Vlachopoulos, N.; Gorlov, M.; Kloo, L. Liquid Electrolytes for Dye-Sensitized Solar Cells. *Dalton Trans.* **2011**, *40*, 10289–10303.

(7) Wu, J.; Lan, Z.; Lin, J.; Huang, M.; Huang, Y.; Fan, L.; Luo, G. Electrolytes in Dye-Sensitized Solar Cells. *Chem. Rev.* **2015**, *115*, 2136–2173.

(8) Papageorgiou, N.; Athanassov, Y.; Armand, M.; Bonhote, P.; Pettersson, H.; Azam, A.; Grätzel, M. The Performance and Stability of Ambient Temperature Molten Salts for Solar Cell Applications. *J. Electrochem. Soc.* **1996**, *143*, 3099–3108.

(9) Wang, P.; Zakeerduddin, S. M.; Exnar, I.; Grätzel, M. High Efficiency Dye-Sensitized Nanocrystalline Solar Cells Based on Ionic Liquid Polymer Gel Electrolyte. *Chem. Commun*. **2002**, 0, 2972–2973.

(10) Wang, P.; Zakeeruddin, S. M.; Comte, P.; Exnar, I.; Grätzel, M. Gelation of Ionic Liquid-Based Electrolytes with Silica Nanoparticles for Quasi-Solid-State Dye-Senistized Solar Cells. *J. Am. Chem. Soc*. **2003**, *125*, 1166–1167.

(11) Cao, Y.; Zhang, J.; Bai, Y.; Li, R.; Zakeeruddin, S. M.; Grätzel, M.; Wang, P. Dye-Sensitized Solar Cells with Solvent-Free Ionic Liquid Electrolytes. *J. Phys. Chem. C* **2008**, *112*, 13775–13781.

(12) Kitazawa, Y.; Iwata, K.; Kido, R.; Imaizumi, S.; Tsuzuki, S.; Shinoda, W.; Ueno, K.; Mandai, T.; Kokubo, H.; Dokko, K.; Watanabe, M. Polymer Electrolytes Containing Solvate Ionic Liquids: A New Approach to Achieve High Ionic Conductivity, Thermal Stability, and a Wide Potential Window. *Chem. Mater.* **2018**, *30*, 252–261.

(13) Bandara, T. M. W. J.; Ajith DeSilva, L. A.; Ratnasekera, J. L.; Hettiarachchi, K. H.; Wijerathna, A. P.; Thakurdesai, M.; Preston, J.; Albinsson, I.; Mellander, B.–E. High Efficiency Dye-Sensitized Solar Cell Based on a Novel Gel Polymer Electrolyte Containing RbI and Tetrahexylammonium Iodide (Hex_4NI) Salts and Multi-Layered Photoelectrodes of TiO_2 Nanoparticles. *Renew. Sust. Energy Rev*. **2019**, *103*, 282–290.

(14) Kojima, A.; Teshima, K.; Shirai, Y.; Miyasaka, T. Organometal Halide Perovskites as Visible-Light Sensitizers for Photovoltaic Cells. *J. Am . Chem. Soc*. **2009**, *131*, 6050–6051.

(15) Im, J.-H.; Lee, C.-R.; Lee, J.-W.; Park, S.-W.; Park, N.-G. 6.5% Efficient Perovskite Quantum-Dot-Sensitized Solar Cell. *Nanoscale* **2011**, *3*, 4088-4093.

(16) Heo, J.; Im, S.; Noh, J.; Mandal, T.; Lim, C.; Chang, J.; Lee, Y.; Kim, H.; Sarkar, A.; Nazeeruddin, M.; Graetzel, M.; Seok, S. Efficient Inorganic–Organic Hybrid Heterojunction Solar Cells Containing Perovskite Compound and Polymeric Hole Conductors. *Nature Photonics* **2013**, *7*, 486–491.

(17) Yang, W. S.; Park, B.-W.; Jung, E. H.; Jeon, N. J.; Kim, Y. C.; Lee, D. U.; Shin, S. S.; Seo, J.; Kim, E. K.; Noh, J. H. Iodide Management in Formamidinium-Lead-Halide-Based Perovskite Layers for Efficient Solar Cells. *Science* **2017**, *356*, 1376–1379.

(18) Appetecchi, G. B.; Croce, F.; Scrosati, B. Kinetics and Stability of the Lithium Electrode in Poly(Methyl methacrylate)-Based Gel Electrolytes. *Electrochim. Acta* **1995**, *40*, 991–997.

(19) Bharwal, A. K.; Manceriu, L.; Alloin, F.; Iojoiu, C.; Dewalque, J.; Toupance, T.; Henrist, C. Bimodal Titanium Oxide Photoelectrodes with Tuned Porosity for Improved Light Harvesting and Polysiloxane-based Polymer Electrolyte Infiltration. *Solar Energy* **2019**, *178*, 98–107.

(20) Karthika, P.; Ganesan, S.; Thomas, A,; Rani, T. M. S.; Prakash, M. Influence of Synthesized Thiourea Derivatives as a Prolific Additive with Tris (1,10-phenanthroline) Cobalt (II/III) Bis / Tris(Hexafluorophosphate) / Hydroxypropyl Cellulose Gel Polymer Electrolytes on Dye-sensitized Solar Cells. *Electrochim. Acta* **2019**, *298*, 237–247.

(21) Choi, B. K.; Kim, Y. W.; Shin, H. K. Ionic Conduction in PEO–PAN Blend Polymer Electrolytes. *Electrochim. Acta* **2000**, *45*, 1371–1374.

(22) Stephan, A. M.; Renganathan, N. G.; Kumar, T. P.; Thirunakaran, R.; Pitchumani, S.; Shrisudersan, J.; Muniyandi, N. Ionic Conductivity Studies on Plasticized PVC/PMMA Blend Polymer Electrolyte Containing $LiBF_4$ and $LiCF_3SO_3$. *Solid State Ionics* **2000**, *130*, 123–132.

(23) Nogueira, A. F.; Durrant, J. R.; De Paoli, M. A. Dye-Sensitized Nanocrystalline Solar Cells Employing a Polymer Electrolyte. *Adv. Mater.* **2001**, *13*, 826–830.

(24) Kubo, W.; Murakoshi, K.; Kitamura, T.; Yoshida, S.; Haruki, M.; Hanabusa, K.; Shirai, H.; Wada, Y.; Yanagida, S. Quasi-Solid-State Dye-Sensitized TiO_2 Solar Cells: Effective Charge Transport in Mesoporous Space Filled with Gel Electrolytes Containing Iodide and Iodine. *J. Phys. Chem. B* **2001**, *105*, 12809–12815.

(25) Yang, Y.; Zhou, C.-H.; Sheng, X.; Hu, H.; Chen, B.-L.; Zhang, J.; Wu, S.; Liu, W.; Zhao, X.-Z. Improved Stability of Quasi-Solid-State Dye-Sensitized Solar Cell Based on Poly(ethylene oxide)–Poly(vinylidene fluoride) Polymer-Blend Electrolytes. *J. Power Sources* **2008**, *185*, 1492–1498.

(26) Yang, H.; Huang, M.; Wu, J.; Lan, Z.; Hao, S.; Lin, J. The Polymer Gel Electrolyte Based on Poly(methyl methacrylate) and Its Application in Quasi-Solid-State Dye-Sensitized Solar Cells. *Mater. Chem. Phys.* **2008**, *110*, 38–42.

(27) Shen, S.-Y.; Dong, R.-X.; Shih, P.-T.; Ramamurthy, V.; Lin, J.-J.; Ho, K.-C. Novel Polymer Gel Electrolyte with Organic Solvents for Quasi-Solid-State Dye-Sensitized Solar Cells. *ACS Appl. Mater. Interfaces* **2014**, *6*, 18489–18496.

(28) Suzuka, M.; Hayashi, N.; Sekigushi, T.; Sumioka, K.; Takata, M.; Hayo, N.; Ikeda, H.; Oyaizu, K.; Nishide, H. A Quasi-Solid State DSSC with 10.1% Efficiency through Molecular Design of the Charge-Separation and -Transport. *Sci. Reports* **2016**, *6*, 28022.

(29) Ming, N. H.; Ramesh, S.; Ramesh, K. The Potential of Incorporation of Binary Salts and Ionic Liquid in P(VP-co-VAc) Gel Polymer Electrolyte in Electrochemical and Photovoltaic Performances. *Sci. Reports* **2016**, *6*, 27630.

(30) Arof, A. K.; Noor, I.M.; Buraidah, M. H.; Bandara, T. M. W. J.; Careem, M. A. Albinsson, I.; Mellander, B.-E. Polyacrylonitrile Gel Polymer Electrolyte Based Dye Sensitized Solar Cells for a Prototype Solar Panel. *Electrochim. Acta* **2017**, *251*, 223–234.

(31) Al-Mohsin, H. A.; Mineart, K. P.; Armstrong, D. P.; E.-S. Ahmed; Spontak, R. J. Quasi-Solid-State Dye-Sensitized Solar Cells Containing a Charged Thermoplastic Elastomeric Gel Electrolyte and Hydrophilic/phobic Photosensitizers. *Sol. RRL* **2018**, 1700145.

(32) Senthil, R. A.; Theerthagiri, J.; Madhavan, J.; Arof, A. K. (2015). Influence of Pyrazole on The Photovoltaic Performance of Dye-sensitized Solar Cell with Polyvinylidene Fluoride Polymer Electrolytes. *Ionics* **2015**, *22*, 425–433.

(33) Buraidah, M. H.; Shah, S.; Teo, L. P.; Chowdhury, F. I.; Careem, M. A.; Albinsson, I.; Mellander, B.-E.; Arof, A. K. High Efficient Dye Sensitized Solar Cells Using Phthaloylchitosan Based Gel Polymer Electrolyte. *Electrochim. Acta* **2017**, *245*, 846–853.

(34) Croce, F.; Appetecchi, G.; Persi, L.; Scrosati, B. Nanocomposite Polymer Electrolytes for Lithium Batteries. *Nature* **1998**, 394, 456–458.

(35) Abraham, K. M.; Alamgir, M. Li^+-Conductive Solid Polymer Electrolytes with Liquid-Like Conductivity. *J. Electrochem. Soc.* **1990**, *137*, 1657–1658.

(36) Huq, R.; Koksbang, R.; Tonder, P. E.; Farrington, G. C. Effect of Plasticizers on the Properties of New Ambient Temperature Polymer Electrolyte. *Electrochim. Acta* **1992**, *37*, 1681–1684.

(37) Akashi, H.; Sekai, K.; Tanaka, K. A Novel Fire-Retardant-Polyacrylonitrile-Based Gel Electrolyte for Lithium Batteries. *Electrochim. Acta* **1998**, *43*, 1193–1197.

(38) Park, J. H.; Cho, J. H.; Lee, E. H.; Kim, J. M.; Lee, S. Y. Conductivity Enhancement of Polyacrylonitrile-Based Electrolytes by Addition of Cascade Nitrile Compounds. *J. Power Sources* **2000**, *90*, 33–38.

(39) Garche, J.; Dyer, C. K.; Moseley, P. T.; Ogumi, Z. Rand, D. A. J.; Scrosati, B. *Encyclopedia of Electrochemical Power Sources.* Newnes: Massachusetts, USA, **2013**.

(40) Wu, G.; Yang, H. Y.; Chen, H. Z.; Yuan, F.; Yang, L. G.; Wang, M.; Fu, R. J. Novel Porous Polymer Electrolyte Based on Polyacrylonitrile. *Mater. Chem. Phys.* **2007**, *104*, 284–287.

(41) Amaral, F. A.; Dalmolin, C.; Canobre, S. C.; Bocchi, N.; Rocha-Filho, R. C.; Biaggio, S. R. Electrochemical and Physical Properties of Poly(Acrylonitrile)/Poly(Vinyl Acetate)-Based Gel Electrolytes for Lithium Ion Batteries. *J. Power Sources* **2007**, *164*, 379–385.

(42) Raghavan, P.; Zhao, X.; Shin, C.; Baek, D. H.; Choi, J. W.; Manuel, J.; Heo, M. Y.; Ahn, J. H.; Nah, C. Preparation and Electrochemical Characterization of Polymer Electrolytes Based on Electrospun Poly(Vinylidene Fluoride-co-hexafluoropropylene)/Polyacrylonitrile Blend/Composite Membranes for Lithium Batteries. *J. Power Sources* **2010**, *195*, 6088–6094.

(43) Wang, S.-H.; Kuo, P.L.; Hsieh, C.-T.; Teng, H. Design of Poly(Acrylonitrile)-Based Gel Electrolytes for High Performance Lithium Ion Batteries. *ACS Appl. Mater. Interfaces* **2014**, *6*, 19360–19370.

(44) Crossland, E. J. W.; Nedelcu, M.; Ducati, C.; Ludwigs, S.; Hillmyer, M. A.; Steiner, U.; Snaith, H. J. Block Copolymer Morphologies in Dye-Sensitized Solar Cells: Probing the Photovoltaic Structure–Function Relation. *Nano Lett.* **2009**, *9*, 2813–2819.

(45) Singh, P. K.; Bhattacharya, B.; Nagarale, R. K. Effect of Nano-TiO_2 Dispersion on PEO Polymer Electrolyte Property. *J. Appl. Polym. Sci.* **2010**, *118*, 2976–2980.

(46) Yang, Y.; Hao, H.; Zhou, C.-H.; Xu, Sheng.; Sebo, B.; Zhao, X.-Z. Novel Agarose Polymer Electrolyte for Quasi-Solid State Due-Sensitized Solar Cell. *J. Power Sources* **2011**, *196*, 2410–2415.

(47) Yang, Y.; Cui, J.; Yi, P.; Zheng, X.; Guo, X.; Wang, W. Effects of Nanoparticle Additives on Agarose Polymer Electrolytes. *J. Power Sources* **2014**, *248*, 988–993.

(48) Chang, W.-C.; Sie, S.-Y.; Yu, W.-C.; Lin, Y.-L.; Yu, Y.-J. Preparation of Nanocomposite Gel Electrolytes with Metal Oxide Additives for Dye-Sensitized Solar Cells. *Electrochim. Acta* **2016**, *212*, 333–342.

(49) Venkatesan, S.; Liu, I.-P.; Chen, L.-T.; Hou, Y.-C.; Li, C.-W.; Lee, Y.-L. Effects of TiO_2 and TiC Nanofillers on the Performance of Dye Sensitized Solar Cells Based on the Polymer Gel Electrolyte of a Cobalt Redox System. *ACS Appl. Mater. Interfaces* **2016**, *8*, 24559–24566.

(50) Zebradstan, N.; Khanmirzaei, M. H.; Ramesh, S.; Ramesh, K. Performance Enhancement of Poly(vinylidene fluoroide-*co*-hexafluoropropylene)/Polyethylene Oxide Based Nanocomposite Polymer Electrolytes with ZnO Nanofiller for Dye-Sensitized Solar Cell. *Org. Electronics* **2017**, *49*, 292–299.

(51) Latip, N. A. A.; Ng, H. M.; Farah, N.; Ramesh, K.; Ramesh, S.; Ramesh, S. Novel Development Towards Preparation of Highly Efficient Ionic Liquid Based Co-Polymer Electrolytes and Its Application in Dye-Sensitized Solar Cells. *Org. Electronics* **2017**, *41*, 33–41.

(52) Sethupathy., M.; Pandey, P. Evaluation of Photovoltaic Efficiency of DSSC Fabricated with Electrospun PVDF–PAN–Fe_2O_3 Composite Membrane. *J. Appl. Polymer.* **2014**, 41107.

(53) Sethupathy, M.; Pandey, P. Photovoltaic Performance of DSSC Fabricated with Polyvinylidene Fluoride–Polyacrylonitrile–Silicondioxide Hybrid Composite Membrane. *Mater. Chem. Phys.* **2014**, *143*, 1191–1198.

(54) Lee, Y-L.; Shen, Y-J.; Yang, Y-M. A Hybrid PVDF–HFP/Nanoparticle Gel Electrolyte for Dye-Sensitized Solar Cell Applications. *Nanotech.* **2008**, *19*, 455201.

(55) Pullanjiot, N.; Swaminathan, S. Enhanced Electrochemical Properties of Metal Oxide Interspersed Polymer Gel Electrolyte for QSDSSC Application. *Solar Energy* **2019**, *186*, 37–45.

(56) Sonker, R. K.; Sbhajeet, R. S. R. ZnO Nanoneedle Structure Based Dye-Sensitized Solar Cell Utilizing Solid Polymer Electrolyte. *Mater. Lett.* **2018**, *233*, 133–136.

(57) Liow, K. S.; Sipaut, C. S.; Jafarzadeh, M. Polypyrrole- and Polyaniline-Surface Modified Nanosilica as Quasi-Solid-State Electrolyte Ingredients for Dye-Sensistized Solar Cells. *J. Mater. Sci. Mater. Electronics* **2018**, *29*, 21907–21108.

(58) Geng, Y.; Sun, X.; Cai, Q.; Shi, Y.; Li, H. Gel Electrolytes Containing Several Kinds of Particles Used in Quasi-Solid-State Dye-Sensitized Solar Cells. *Rare Metals* **2006**, *25*, 201–206.

(59) Bella, F.; Popovic, J.; Lamberti, A.; Tresso, E.; Gerbaldi, C.; Maier, J. Interfacial Effects in Solid-Liquid Electrolytes for Improved Stability and Performance of Dye-Sensitized Solar Cells. *ACS Appl. Mater. Int.* **2017**, *9*, 37797–37803.

(60) Wang, X.; Kulkarni, S.; Ito, B.; Batabyal, S.; Nonomura, K.; Wong, C.; Gratzel, M.; Mhaisalkar, S.; Uchida, S. Nanoclay Gelation Approach Toward Improved Dye-Sensitized Solar Cell Efficiencies: An Investigation of Charge Transport and Shift in the TiO_2 Conduction Band. *ACS Appl. Mater. Interfaces* **2013**, *5*, 444–450.

(61) Wang, X.; Deng, R.; Kulkarni, S.; Wang, X.; Pramana, S.; Wong, C.; Gratzel, M.; Uchida, S.; Mhaisalkar, S. Investigation of the Role of Anions in Hydrotalcite for Quasi-Solid State Dye-Sensitized Solar Cells Application. *J. Mater. Chem. A* **2013**, *1*, 4345–4351.

(62) Andrade, Jr., M. A. S.; Tiihonen, A.; Miettunen, K.; Lund, P.; Nogueria, A. F.; Pastore, H. O. Gel Electrolytes with Polyamidopyridine Dendron Modified Talc for Dye-Sensitized Solar Cells. *ACS Appl. Mater. Interfaces* **2017**, *9*, 20454–20466.

(63) Lee, C.; Chen, P.; Vittal, R.; Ho, K. Iodine-Free high Efficient Quasi Solid-State Dye-Sensitized Solar Cell Containing Ionic Liquid and Polyaniline-Loaded Carbon Black. *J. Mater. Chem.* **2010**, *20*, 2356–2561.

(64) Wang, Y.; Huang, K.; Dong, R.; Liu, C.; Wang, C.; Ho, K.; Lin, J. Polymer-Dispersed MWCNT Gel Elecrolytes for High Performance of Dye-Sensitized Solar Cells. *J. Mater. Chem.* **2012**, *22*, 6982–6989.

(65) Akhtar, M.; Kwon, S.; Stadler, F.; Yang, O. High Efficiency Solid State Dye Sensitized Solar Cells with Graphene–Polyethylene Oxide Composite Electrolytes. *Nanoscale* **2013**, *5*, 5403–5411.

(66) Prabakaran, K.; Mohanty, Sm.; Nayak, S. K. Improved Electrochemical and Photovoltaic Performance of Dye Sensitized Solar Cells Based on PEO/PVDF–HFP/Silane Modified TiO_2 Electrolytes and MWCNT/Nafion® Counter Electrode. *RSC Adv.* **2015**, *5*, 40491–40504.

(67) Yang, Y.; Yi, P.; Zhou, C.-H.; Cui, J.; Zheng, X.; Xiao, S.; Guo, X.; Wang, W. Magnetic Field Processed Solid-State Dye-Sensitized Solar Cells with Nickel Oxide Modified Agarose Electrolyte. *J. Power Sources* **2013**, *243*, 919–924.

(68) Guo, X.; Yi, P.; Yang, Y.; Cui, J.; Xiao, S.; Wang, W. Effects of Surfactants on Agarose-Based Magnetic Polymer Electrolyte for Dye-Sensitized Solar Cells. *Electrochim. Acta* **2013**, *90*, 524–529.

(69) Xiao, S.; Cui, J.; Yi, P.; Yang, Y.; Guo, X. Insights Into Electrochemical Properties of Co_3O_4-Modified Magnetic Polymer Electrolyte. *Electrochim. Acta* **2014**, *144*, 221–227.

(70) Yang, Y.; Gao, J.; Yi, P.; Cui, J.; Guo, X. The Influence of Co_3O_4 Concentration on Quasi-Solid-State Dye-Sensitized Solar Cells with Polymer Electrolyte. *Solid State Ionics* **2015**, *279*, 1–5.

(71) Chou, T. P.; Zhang, Q.; Russo, B.; Fryxell, G. E.; Cao, G. Titania Particle Size Effect on the Overall Performance of Dye-Sensitized Solar Cells. *Phys. Chem. C*, **2007**, *111*, 6296–6302.

(72) Ali, F. H.; Alwan, D. B. Effect of Particle Size of TiO_2 and Additive Materials to Improve Dye Sensitized Solar Cells Efficiency. *IOP J. Physics: Conf. Series* **2018**, *1003*, 012077.

(73) Kumar, R. V.; Diamant, Y.; Gedanken, A. Sonochemical Synthesis and Characterization of Nanometer-Size Transition Metal Oxides from Metal Acetates. *Chem. Mater.* **2000**, *2301*–2305.

(74) Chen, S.; Kumar, R. V.; Gedanken, A.; Zaban, A. Sonochemical Synthesis of Crystalline Nanoporous Zinc Oxide Spheres and Their Application in Dye-Sensitized Solar Cells. *Isr. J. Chem.* **2001**, *41*, 51–54.

(75) Yu, J. C.; Zhang, L.; Yu, J. Direct Sonochemical Preparation and Characterization of Highly Active Mesoporous TiO_2 with a Bicrystalline Framework. *Chem. Mater.* **2002**, *14*, 4647–4653.

(76) He, C.-X.; Lei, B.-X.; Wang, Y.-F.; Su, C.-Y.; Fang, Y.-P.; Kuang, D.-B. Sonochemical Preparation of Hierarchical ZnO hollow Spheres for Efficient Dye-Sensitized Solar Cells. *Chem. Eur. J.* **2010**, *16*, 8757–8761.

(77) Ramachandran, R.; Jung, D.; Bernier, N. A.; Logan, J. K.; Waddington, M. A.; Spokoyny, A. M. Sonochemical Synthesis of Small Boron Oxide Nanoparticles. *Inorg. Chem*. **2018**, *57*, 8037–8041.

(78) Kawaoka, H.; Hibino, M.; Zhou, H.; Honma, I. Sonochemical Synthesis of Amorphous Manganese Oxide Coated Carbon and Application to High Power Battery. *J. Power. Sources.* **2004**, *125*, 85–89.

(79) Xing, Y. Synthesis and Electrochemical Characterization of Uniformly-Dispersed High Loading Pt Nanoparticles on Sonochemically-Treated Carbon Nanotubes. *J. Phys. Chem. B* **2004**, *2004*, 19255–19259.

(80) Kamar, E. M.; Reda, S. M. Sonochemical Method for Synthesizing Co_3O_4/Graphene Nanocomposites for Use as Counter Electrode in Dye-Sensitized Solar Cells. *Appl. Phys. A* **2016**, *122*, 688.

(81) Ming, N.H.; Ramesh, S.; Ramesh, K. Exploration on the P(VP-*co*-VAc) Copolymer Based Gel Polymer Electrolytes Doped with Quaternary Ammonium Iodide Salt for DSSC Applications: Electrochemical Behaviors and Photovoltaic Performances. *Org. Electronics* **2015**, *22*, 132–139.

(82) Suganthi, K. S.; Rajan, K. S. Effect of Calcination Temperature on the Transport Properties and Colloidal Stability of ZnO–Water Nanofluids. *Asian J. Sci. Res.* **2012**, *5*, 207–217.

(83) Omar, F. S.; Numan, A.; Duraisamy, N.; Bashir, S.; Ramesh, K.; Ramesh, S. Ultrahigh Capacitance of Amorphous Nickel Phosphate for Asymmetric Supercapacitor Applications. *RSC Adv.* **2016**, 6, 76298–76306.

(84) Smith, S. J.; Huang, B.; Liu, S.; Liu, Q.; Olsen, R. E.; Boerio-Goates, J.; Woodfield, B. F. Synthesis of Metal Oxide Nanoparticles via a Robust 'Solvent-Deficient' Method. *Nanoscale* **2016**, *7*, 144–156.

(85) Nadarajan, R.; Bakar, W. A. W. A.; Ali, R. Effect of Calcination Temperature on Metal Oxides and Their Photocatalytic Activity. *Adv. Mater. Res.* **2015**, *1107*, 73–78.

(86) Saidi, N. M.; Ng, H. M.; Omar, F. S.; Bashir, S.; Ramesh, K.; Ramesh, S. Polyacrylonitrile–poly(1-vinyl pyrrolidone-co-vinyl acetate) Blend Based Gel Polymer Electrolytes Incorporated with Sodium Iodide Salt for Dye-Sensitized Solar Cell Applications. *J. Appl. Polym. Sci.* **2019**, *136*, 47810.

(87) Patterson, A. L.; The Scherrer Formula for X-Ray Particle Size Determination. *Phys. Rev.* **1939**, *56*, 978.

(88) Klig, H.; Alexander, L. *X-Ray Diffraction Procedures*. Wiley: New York, USA, **1962**.

(89) Perrin, A.; Myers, D.; Fucke, K.; Musa, O. M.; Steed, J. W. *N*-Alkyl Pyrrolidone Ether Podands as Versatile Alkali Metal Ion Chelants. *Dalton Trans.* **2014**, *43*, 3153–3161.

(90) Arrhenius, S. A. Z. On the Reaction Rate of the Inversion of Non-Refined Sugar Upon Souring. *Z. Phys. Chem.* **1889**, *4*, 226–248.

(91) Ratner, M.; Shriver, D. Ion Transport in Solvent-Free Polymers. *Chem. Rev.* **1988**, *88*, 109–124.

(92) Vogel, H. The Law of the Relationship Between Viscosity of Liquids and the Temperature. *Phys. Z.* **1921**, *22*, 645–646.

(93) Thammann, G.; Hesse, W. Die Abhängigkeit der Viscosität von der Temperatur bie unterkühlten Flüssigkeiten. *Z. Anorg. Allg. Chem.* **1926**, *156*, 245–250.

(94) Fulcher, G. S. Analysis of Recent Measurements of the Viscosity of Glasses. *J. Am. Ceram. Soc*. **1925**, *8*, 339–355.

(95) Kawano, R.; Watanabe, M. Equilibrium Potentials and Charge Transport of an I^-/I_3^- Redox Couple in an Ionic Liquid. *Chem. Commun.* **2003**, 330–331.

(96) Aziz, S. B.; Woo, T. J.; Kadir, M. F. Z.; Ahmed, H. M. A Conceptual Review on Polymer Electolytes and Ion Transport Models. *J. Sci: Adv. Mater. Devices* **2018**, *3*, 1–17.

(97) Son, Y. J.; Kang, J. S.; Yoon, J.; Kim, J.; Jeong, J. Kang, J.; Lee, M. J.; Park, H. S.; Sung, Y.-E. Influence of TiO_2 Particle Size on Dye-Sensitized Solar Cells Employing an Organic Sensitizer and a Cobalt(III/II) Redox Electrolyte. *J. Phys. Chem. C* **2018**, *122*, 7051–7060.

(98) Braja, D.; Ghosh, K.; Lott, J.; Ritchie, E. Conductivity Dependence of PEG Content in an Anhydrous Proton Conducting Sol–Gel Electrolyte. *Chem. Mater*. **2005**, *17*, 661–669.

(99) Zhang, K.; Cui, Z.; Xing, G.; Feng, Y.; Meng, S. Improved Performance of Dye-Sensitized Solar Cells Based on Modified Kaolin/PVDF-HFP Composite Gel Electrolytes. *RSC Adv.*, **2016**, *6*, 100079–100089.

(100) Sarker, S.; Ahammad, A. J. S.; Seo, H. W.; Kim, D. M. Electrochemical Impedance Spectra of Dye-Sensitized Solar Cells: Fundamentals and Spreadsheet Calculation. *Int. J. Photoenergy* **2014**, *2014*, 851705.

Table of Contents (TOC) Graphic